Microcalorimeter Magnetic Sensor Geometries Using Superconducting Elements

STP Boyd[a] and RH Cantor[b]

[a]*University of New Mexico, MSC07 4220, Albuquerque NM 87131-0001 USA*
[b]*STAR Cryoelectronics, 25-A Bisbee Ct., Santa Fe NM 87508-1338 USA*

Abstract. We describe a numerical code developed to estimate performance of magnetic microcalorimeter configurations, including superconducting elements and SQUID characteristics. We present results of a preliminary design analysis showing that composite sensors with both superconducting and paramagnetic elements should realize substantial gains in magnetic flux signal per magnetization change of the paramagnet, compared to sensors containing only paramagnet.

Keywords: microcalorimeter, radiation detector, thin-film, SQUID
PACS: 29.40.Vj, 07.55.Jg, 85.25.Am, 85.70.Kh, 07.85.Nc

INTRODUCTION

Microcalorimetry using metallic paramagnetic sensors is a powerful new technique that brings new physics to the problem of particle detection(1). With that new physics comes new constraints and new degrees of freedom in sensor design. Performance is dependent on the detailed geometry of the paramagnet and the pickup and magnetizing coils. In this report we present a preliminary study of the effect of including superconducting elements in that geometry.

NUMERICAL MODEL

The numerical models were constructed using COMSOL Multiphysics(2). All models presented are 2D axisymmetric. Aluminum is assumed as the superconductor(3).

Several simplifications were made for this introductory study.

The temperature– and field–dependent heat capacity and relative magnetic permeability of the paramagnet were calculated using a previously-developed simplified model(4)(5). This model assumes noninteracting spins with g and J values previously determined by others for Fe in a Pd matrix, plus the linear term of the electronic specific heat of Pd. For the lowest temperature available to us, T_{nom}=50mK, the paramagnet model shows that the maximum magnetization responsivity will be obtained in a magnetizing field of B_{nom}=3.0mT.

No attempt was made to include the internal dynamics of the sensor, which should properly include time constants for the equilibration of the conduction electrons with the spins(1) and for the superconductor with the paramagnet.

The present simplified model should suffice for the relative comparisons of different sensor configurations presented here, but the absolute noise values should not be considered accurate. We plan to correct these simplifications in future work.

A typical calculation for a given sensor geometry proceeds in four steps.

First, the nominal operating current for the magnetizing coil I_{nom} is found. A nonlinear magnetostatic solution is obtained at the nominal operating temperature T_{nom} using a trial current I_{trial}. The volumetric mean field in the paramagnet $\overline{B}_{para}$ is found, and I_{trial} is scaled $I_{trial} \rightarrow I_{trial}\left(B_{nom}/\overline{B}_{para}\right)$. This relaxation procedure is iterated to allow for the nonlinearity of the paramagnet. Typically three cycles yields $\overline{B}_{para} = B_{nom}$ to 3 significant figures.

Second, nonlinear magnetostatic solutions using the determined I_{nom} are obtained at a series of temperatures, starting at T_{nom} and increasing in logarithmically-spaced steps. At each temperature the quantities determined are: C_{sensor}, the summed heat capacities of the composite sensor; E_{total}, the total magnetic energy in the system; and ϕ_{pickup} and ϕ_{mag}, the fluxes linked to the pickup and magnetizing coils, respectively. Using these quantities we calculate: the

self-inductance of the magnetizing coil $L_{mag} = 2E_{total}/I_{nom}^2$; the sensor energy corresponding to each temperature $E_{sensor} = \int C_{sensor}\,dT$, where the integral is approximated; the mean flux/energy responsivity at the pickup coil $\rho_{pickup} = \Delta\phi_{pickup}/\Delta E_{sensor}$, where the deltas are taken from the operating point values; and a useful figure of merit we call the "magnetic efficiency"

$$\varepsilon = \Delta\phi_{pickup}/\left(\Delta\bar{\mu}_r \cdot \bar{B} \cdot V\right), \qquad (1)$$

where all quantities in the denominator are evaluated in the paramagnet (V is the paramagnet volume).

Typically ρ_{pickup} versus ΔE_{sensor} rolls off with a well-defined shoulder on a log-log plot, so we determine a "saturation energy" for the sensor at which ρ_{pickup} is down by 3dB.

Third, a series of linear harmonic solutions with the pickup coil excited by current I_{pickup} are obtained at logarithmically-spaced frequencies spanning a range exceeding the bandwidth of the device. The pickup and magnetizing coils may be the same coil. The relative magnetic permeability μ_r of the paramagnet in these calculations is set constant at the paramagnet volume average $\bar{\mu}_r$ obtained in the nonlinear magnetostatic solution at T_{nom} and B_{nom}. This simplification speeds the calculations considerably and is well-justified by the observed small spatial variation of μ_r.

At each frequency we find the eddy-current power dissipated in the sensor P_{sensor} and the back-EMF of the pickup coil V_{pickup}. From these quantities we determine the effective resistance of the pickup coil $R_{pickup}(f) = P_{sensor}(f)/I_{pickup}^2$, and its self-inductance $L_{pickup}(f) = \Im\left(V_{pickup}(f)\right)/\left(dI_{pickup}/dt\right)$. The self-inductance L_{pickup} is constant up to a frequency f_{skin} where it starts to decrease as the skin depth becomes comparable to the paramagnet thickness. Because R_{pickup} results from eddy currents, R_{pickup}/f^2 is also constant until it starts to fall for $f > f_{skin}$.

The final step in the calculation is the estimation of noise spectra. The code can estimate noise spectra for either specific SQUID characteristics, or for "optimal SQUIDs," which are assumed to have an input coil with inductance exactly matched to the low-frequency limit of L_{pickup} and a realistic 0.9 coefficient of coupling to a 100pH SQUID loop. For all SQUID configurations we assume a high-bandwidth device using two-stage SQUID amplification yielding a generic single-pole flux noise spectrum similar to what we have seen with our micro-susceptometer(4)(5)

$$\phi_{SQUID}(f) = \phi_{SQUID}^{LF}\Big/\sqrt{1+\left(f/f_{SQUID}^{shoulder}\right)^2}.$$

with the low-frequency limit ϕ_{SQUID}^{LF}=0.8μΦ$_0$/√Hz and shoulder frequency $f_{SQUID}^{shoulder}$=1.4MHz.

The thermal fluctuation noise (TFN) is developed in the usual way from the fluctuation-dissipation theorem(6), assuming a thermal RC circuit and frequency-independent $R_{thermal}$ and C_{sensor}. For each geometry $R_{thermal}$ is adjusted to achieve a thermal shoulder frequency of 100KHz with the calculated C_{sensor}. This gives the TF flux noise spectrum at the pickup coil as

$$\phi_{pickup}^{TF}(f) = \frac{\rho_{pickup} C_{sensor}\sqrt{4k_B T^2 R_{thermal}}}{\sqrt{1+\left(2\pi f R_{thermal} C_{sensor}\right)^2}}.$$

To determine the TF flux noise spectrum at the SQUID we must account for the response of the input circuit, which has both resistance (due to eddy power dissipation) and inductance. We first calculate the voltage noise induced across the pickup coil and then solve for the TF flux noise at the SQUID, finding

$$\phi_{SQUID}^{TF}(f) = \frac{\phi_{pickup}^{TF}(f)}{k_{input} L_{total}(f)}\Bigg/\sqrt{1+\left(\frac{R_{pickup}(f)}{2\pi f\, L_{total}(f)}\right)^2} \qquad (2)$$

where

$$L_{total}(f) = L_{pickup}(f) + L_{input} + L_{parasitic}$$

is the total inductance of the input circuit.

The noise due to thermally-induced eddy currents in the metallic paramagnet, the "magnetic Johnson noise," (MJN) is again developed(1) from the fluctuation-dissipation theorem, which states that the MJN can be calculated from the thermal voltage noise across R_{pickup}. As with the TF noise, we again have a voltage noise acting in the input circuit. The MJ flux noise at the SQUID is then

$$\phi_{SQUID}^{MJ}(f) = \frac{\sqrt{4k_B T R_{pickup}(f)}}{k_{input} 2\pi f L_{total}(f)}\Bigg/\sqrt{1+\left(\frac{R_{pickup}(f)}{2\pi f L_{total}(f)}\right)^2}.$$

We now have the total flux noise at the SQUID as

$$\phi_{SQUID}^{total}(f) = \sqrt{\phi_{SQUID}(f)^2 + \phi_{SQUID}^{TF}(f)^2 + \phi_{SQUID}^{MJ}(f)^2}.$$

The flux/energy responsivity at the SQUID ρ_{SQUID} relates this flux noise at the SQUID to equivalent energy noise at the sensor. Eq.(2) gives us $\rho_{SQUID}(f)$ if we substitute ρ_{SQUID} and ρ_{pickup} for ϕ_{SQUID}^{TF} and ϕ_{pickup}^{TF}. If both the skin depth frequency f_{skin} and the low-frequency limit of $2\pi f^2 L_{total}(f)/R_{pickup}(f)$ are above the measurement bandwidth, we obtain the frequency-independent $\rho_{SQUID} = \rho_{pickup}/\left(k_{input} L_{total}\right)$.

RESULTS AND DISCUSSION

Initial application of the new code was to the existing geometry and SQUID characteristics of our miniature SQUID micro-susceptometer, which has been described previously in detail(4)(5). Our focus was not on practical new devices, but to establish a baseline using the new code with the simplified paramagnet model and to take a first look at the impact that composite superconductor/paramagnet sensors could have on device performance.

Within this configuration we studied the three sensor geometries shown in Fig. 1. In Case 1 the sample is a paramagnetic disk with varying height and outer diameter 55μm. In Case 2 the same volume of paramagnet has been arranged as a ring of square cross-section and outer diameter 55μm. Case 3 has the same paramagnet geometry as Case 2, but the volume inside the ring has been filled with superconductor.

Total RMS noise versus saturation energy of the three different configurations is shown in the top part of Fig. 2. Rearranging the paramagnet volume to a ring of square aspect ratio near the pickup loop provides a small enhancement of noise performance at lower saturation energies, but filling the inside of that ring with superconductor provides a great deal more.

One quantitative measure of this improvement is provided by the "magnetic efficiency" (Eq.(1)), which provides a paramagnet-material-independent measure of the quality of a sensor geometry. We see in the lower part of Fig. 2 that the magnetic efficiency of the baseline configuration, Case 1, varies from about 5-20/mm. Case 3, using the superconductor filling, achieves up to about 100/mm.

The geometry of Case 3 has several features that contribute to improved performance. As with Case 2, it reshapes the paramagnet cross-section to an aspect ratio with a smaller demagnetizing factor, and it forms the paramagnet into a ring, which reduces eddy power dissipation, and thus R_{pickup} and MJN. Because of the Meissner effect, the superconductor effectively eliminates all pickup loop area which is not filled by paramagnet. Also because of the Meissner effect, the superconductor does not contribute to MJN. Lastly, for $T/T_c \ll 1$, the superconductor contributes very little to the heat capacity.

Can other geometries containing superconducting elements also achieve or exceed these advantages? One candidate geometry that builds directly on the example of Case 3 would have a thin coating of paramagnet on the outer diameter of a superconducting cylinder, with the magnetizing field parallel to the cylinder axis. This creates a long and thin paramagnet cross-section that can effectively eliminate the

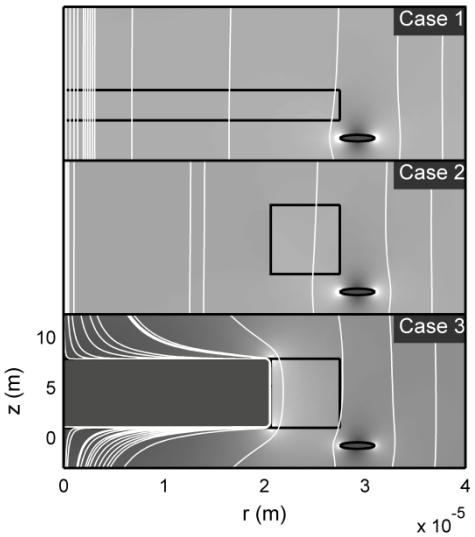

FIGURE 1. The same volume of paramagnet (saturation energy ~90KeV), configured three different ways in the micro-susceptometer. The three pictures show the same view at the same scale. The left boundary is the vertical axis of rotational symmetry, centered in one pickup loop of the micro-susceptometer. The small oval shape at lower right is the pickup coil with inner diameter of 55μm. Shading indicates *B* field magnitude created by the spiral magnetizing coil (out of view to the right in these pictures) ranging from 0 (darkest) to 5mT (white). Magnetic field lines are white.

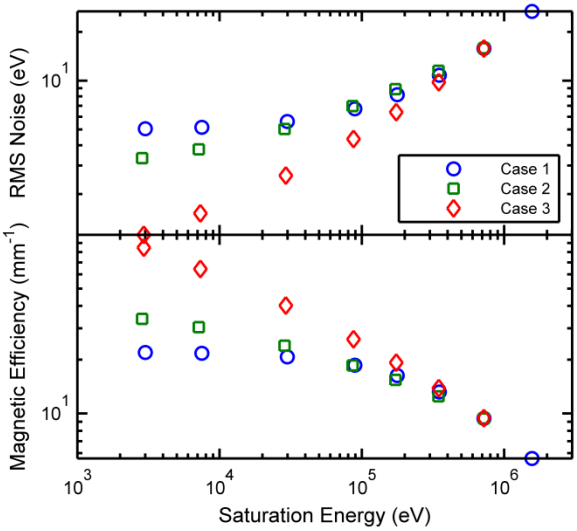

FIGURE 2. Estimated noise and "magnetic efficiency" for the three sensor geometries shown in Fig. 1.

demagnetizing factor. The pickup coil would be multiple turns around the outside of the coated cylinder to maximize the flux change.

We performed exploratory calculations for the coated cylinder geometry, and in fact the results were very good. However, to achieve maximum advantage the turns of the pickup coil need to be very thin, and very closely spaced to each other and to the

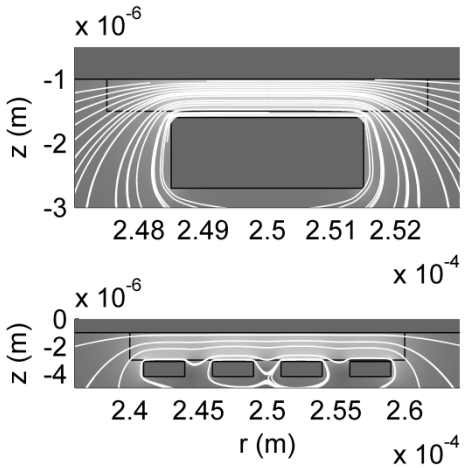

FIGURE 3. "Pancake coil + superconductor" geometry details. (Upper) 0.5μm×5μm paramagnetic film with a 1–turn coil. (Lower) 2μm×20μm paramagnetic film with a 4–turn coil. Coil traces are 1.1μm×3μm, with 2μm spacing. Shading and field lines are as in Fig. 1.

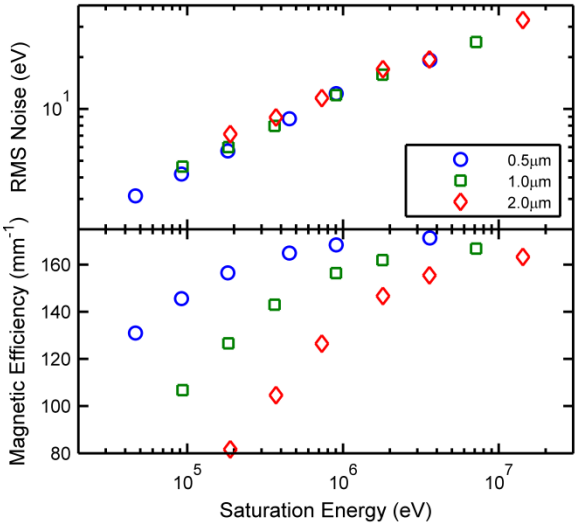

FIGURE 4. Estimated noise and "magnetic efficiency" for "pancake + superconductor" geometries with paramagnetic film thicknesses as indicated.

paramagnet. In short, the best performance would be obtained if the pickup coil turns could be formed with photolithography. This would present a substantial technical challenge.

A photolithographically feasible alternative is offered by the topologically equivalent "pancake coil + superconductor" geometry shown in Fig. 3. The solenoidal pickup/magnetizing coil is flattened to a pancake coil. The paramagnet is a ring-shaped film on top of the pickup coil, and the superconducting cylinder becomes a disk-shaped superconducting cap layer. The magnetizing field along the axis of the cylinder is now directed radially outward from the center of the pancake coil. This geometry differs from meander geometries in that the current in all the turns of the pancake coil is in the same direction, the field builds constructively, all of the paramagnet is used efficiently, and the superconducting cap aligns and concentrates field and reduces pickup loop area to achieve high magnetic efficiency.

Noise (assuming optimal SQUIDs) and magnetic efficiency of this geometry are shown in Fig. 4. The design is promising. Performance should be comparable to the micro-susceptometer approach. The noise estimate at the lowest saturation energy, ~50KeV, is roughly equal to the corresponding noise shown for Case 3 in Fig. 2. Note also that, in contrast to Fig. 2, the magnetic efficiency starts out high at low saturation energies and now *increases* as the saturation energy increases for each paramagnet thickness, so efficient implementation at higher saturation energies should be possible. Note also that the superconducting cap used in Figs. 3 and 4 is 1mm in diameter, so metal-to-metal attachment of a 1mm diameter superconducting absorber should be straightforward.

SUMMARY/FUTURE WORK

Our calculations have identified a promising sensor configuration employing superconducting elements. We plan in the next round of calculations to upgrade the paramagnet properties to measured data, and to further optimize the new configuration for fabrication.

ACKNOWLEDGMENTS

We are grateful to C. Enss and A. and L. Fleischmann for helpful comments and discussions. This work supported by the U.S. Defense Threat Reduction Agency.

REFERENCES

1. A. Fleischmann, C. Enss, and G. M. Seidel, "Metallic Magnetic Calorimeters," in *Cryogenic Particle Detection*, C. Enss, Ed. Berlin: Springer-Verlag, 2005, pp. 151–216.
2. http://comsol.com.
3. N.E. Phillips, *Physical Review* **114**, 676-686 (1959). We use the simple theoretical fit, neglecting his observation of excess heat capacity near 0.1K.
4. S. T. P. Boyd, V. Kotsubo, R.H. Cantor, A. Theodorou, and J.A. Hall, *IEEE Trans. Appl. Super.* **19** (3) (2009).
5. S.T.P. Boyd, R. Cantor, V. Kotsubo, P. Blumenfeld, and J.A. Hall, *J. Low Temp. Phys.* **151**, 369 (2008).
6. H. B. Callen and T. A. Welton, *Physical Review* **83**, 34-40 (1951).